Gold Nanoshell/Polysaccharide Nanofilm for Controlled Laser-Assisted Tissue Thermal Ablation

Eugenio Redolfi Riva,[†,‡,*] Andrea Desii,[†,*] Edoardo Sinibaldi,[†] Gianni Ciofani,[†] Vincenzo Piazza,[§] Barbara Mazzolai,[†] and Virgilio Mattoli[†,*]

[†]Center for Micro-BioRobotics, Istituto Italiano di Tecnologia, Pontedera, 56025, Italy, [‡]The Biorobotics Institute, Scuola Superiore Sant'Anna, Pontedera, 56025, Italy, and [§]Center for Nanotechnology Innovation, Istituto Italiano di Tecnologia, Pisa, 56127, Italy

ABSTRACT We report on the fabrication and characterization of a freestanding ultrathin, mucoadhesive gold nanoshell/polysaccharide multilayer nanocomposite (thermonanofilm, TNF), that can be used for controlled photothermal ablation of tissues through irradiation with near-infrared radiation (NIR) laser. The aim of this work is to provide a new strategy to precisely control particle concentration during photothermalization of cancerous lesions, since unpredictable and aspecific biodistributions still remains the central issue of inorganic nanoparticle-assisted photothermal ablation. Gold nanoshell encapsulation in polysaccharide matrix is achieved by drop casting deposition method combined with spin-assisted layer-by-layer (LbL) assembly. Submicrometric thickness of films ensures tissue adhesion. Basic laser-induced heating functionality has been demonstrated by *in vitro* TNF-mediated thermal ablation of human neuroblastoma cancer cells, evidenced by irreversible damage to cell membranes and nuclei. *Ex vivo* localized vaporization and carbonization of animal muscular tissue is also demonstrated by applying TNF onto tissue surface. Thermal distribution in the tissue reaches a steady state in a few seconds, with significant increases in temperature ($\Delta T > 50$) occurring across an 1 mm span, ensuring control of local photothermalization and providing more safety and predictability with respect to traditional laser surgery. A steady-state model of tissue thermalization mediated by TNFs is also introduced, predicting the temperature distribution being known the absorbance of TNFs, the laser power, and the tissue thermal conductivity, thus providing useful guidelines in the development of TNFs. Thermonanofilms can find applications for local photothermal treatment of cancerous lesions and wherever high precision and control of heat treatment is required.

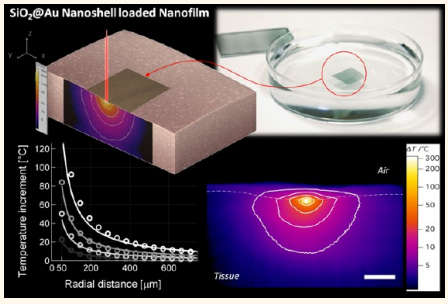

KEYWORDS: nanofilms · layer-by-layer thin films · gold nanoshells · cancer thermal ablation · surface plasmon resonance

The possibility of destroying tumor masses by thermal effect is a safe and nontoxic strategy that can be associated with the current anticancer techniques, such as chemotherapy and radiotherapy.[1] Hyperthermia is a thermal therapeutic strategy against cancer introduced in the early 1970s, based on the induction of cell death caused by a temperature rise of the tumor mass above 43 °C, maintained for several minutes. Heat has a destructive effect on tumor masses because of a lower heat dissipation compared to normal tissue, caused by poor vascularization due to uncontrolled replication of cancer cells,[2] with a consequent increase of the thermal damage toward malignancy rather than healthy tissues.[3] In clinical practice, hyperthermia is used in combination with traditional therapeutic strategies (chemotherapy and radiotherapy).[4] The heat is generated in the target area by using microwave or radiofrequencies applicators inserted within the tumor mass by surgery (*interstitial hyperthermia*),[5] or by using complex devices that concentrate the radiation within an area in depths of the body (*regional* and *part-body hyperthermia*).[6] However, hyperthermia and subsequent cell death induction is not the only feasible heat treatment against cancer. Thermal ablation uses heat to induce different biological effects in tissues: protein denaturation and cell membrane stress ($T = 50-60$ °C), coagulation and necrosis ($T > 60$ °C), tissue carbonization ($T > 100$ °C), pyrolysis and vaporization of solid tissue ($T > 300$ °C).[7] All tissues, even cancerous lesions, can undergo coagulation by one of these mechanisms, since they are not mediated by biochemical processes.

* Address correspondence to eugenio.redolfi@iit.it, andrea.desii@gmail.com, virgilio.mattoli@iit.it.

Received for review December 11, 2013 and accepted May 5, 2014.

Published online May 05, 2014
10.1021/nn406348v

Consequently, the noninvasiveness and efficacy of thermoablative procedures depends on its selectivity toward cancer cells. Continuous or pulsed collimated laser light, (as in PLA, percutaneous laser ablation),[8] radiofrequencies (RFA, radiofrequency ablation)[9] and focused ultrasound waves (HIFU, high intensity focused ultrasound)[10] can provide irreversible thermal damage to cancer cells.

Nanotechnology, with the development of new smart materials, is paving the way for the development of innovative thermal therapeutic strategies against cancer.[11] Superparamagnetic iron oxides nanoparticles (SPIONs) can be accumulated in tumor tissue exploiting its enhanced permeability and retention effect (EPR) to macromolecules and nanoparticles.[12] Hyperthermia of SPION retaining tissues is achieved by magnetization hysteresis losses due to the delay in alignment of the magnetization of single domain particles to an alternating external magnetic field in the radiofrequencies. This technique, called magnetic fluid hyperthermia (MFH), was first presented in a pioneering work by Gordon.[13] The development of accurate thermal models and particle surface modification processes has allowed successful clinical trials of MFH.[14−18]

Tissue heating can be achieved exploiting localized surface plasmon resonance (LSPR) occurring in metal nanocrystals since electron−phonon relaxation causes heat conversion of absorbed light energy.[19] Light absorption by LSPR can be tuned by modifying particle size and morphology.[20,21] As an example, by varying gold nanorod aspect ratio and gold-silica nanoshell core-to-shell ratio it is possible to shift the absorption peak to near-infrared (NIR) wavelength (λ = 700−900 nm), obtaining a photothermal effect under NIR laser irradiation.[22,23] The low absorption coefficient of water and biological tissue toward near-infrared light[24] can be exploited to induce noninvasive photothermalization through nanocrystals retained in deep lesions. In a series of works by the group of Jennifer L. West, the efficacy of nanoshell-mediated photothermalization has been demonstrated. Once irradiated with NIR laser, gold-silica nanoshells are able to destroy human breast carcinoma cells, murine colon carcinoma cells, and human glioma cells, both *in vitro* and *in vivo* in mice.[25−27] Tissue selectivity can be increased to a certain extent by surface functionalization with target ligands[28,29] and encapsulation inside nanocarriers.[30,31] However, the effective dynamic biodistribution of inorganic nanoparticles *in vivo* remains a complex aspect, which is still not completely understood.[32] Particle transport *in vivo* results from various processes and phenomena, as pressure gradient, extravasation from the vascular circuit, diffusion and convection inside extracellular matrix, and cell internalization (endocytosis).[33] During their passage within the bloodstream, particles can undergo clearance by the reticuloendothelial system (RES) or can accumulate in nonspecific regions of the body.[34] Biodistribution studies in rats and mice of gold nanoparticles and other engineered nanomaterials showed that maximum particle concentration was found in blood, lungs, liver, and spleen.[35−37] Control of particle concentration and distribution in cancer tissue still remain a major issue in the clinical application of inorganic nanoparticles.[38,39] In nanocrystal-mediated ablation, the heterogeneous distribution and the inability to readily visualize and quantify particles pose further problems in dosimetry and photothermal modeling.[40]

The use of a nanocomposite implant with controlled particle density could improve the therapeutic efficacy of nanocrystal-mediated photothermal ablation, hampering unspecific biodistribution of particles and improving the control of particle concentration in lesions. NIR-absorbent metal nanocrystals could be incorporated in a free-standing bioadhesive film to obtain stable contact with the surface of a tumor mass. Moreover, NIR-laser exposition can enhance adhesion of such a film in order to improve immobilization in the desired area.[41] Free-standing nanofilms (NF) are polymer films characterized by a thickness of tens of nanometers and lateral sizes in the centimeter range. Their high aspect ratio results in a very low bending stiffness and in an improved adhesion to all kinds of biosurfaces.[42] Various reports propose the biomedical application of polymeric nanofilms as easy-to-handle ultrathin plasters, with wound repairing properties, as a tissue engineering scaffolds for biohybrid actuators, as targeted drug delivery systems and ultraconformable smart interfaces.[43−49] Nanocomposite, free-standing, ultrathin polymer films incorporating nanoparticles can be fabricated by spin-assisted coating of stable dispersions of nanoparticles or as layer-by-layer (LbL) assemblies of alternating polyelectrolytes and charged particles. Carbon nanotubes, metal nanoparticles, SPIONs, and nanoclays are some of the inorganic fillers expolited.[50−56]

The aim of this work is to develop a stable, flexible, and ultrathin polymeric platform based on a LbL assembly of polysaccharides incorporating gold nanoshells. This composite could improve particle manipulation and density control in nanocrystal-mediated photothermal ablation and hyperthermia. Moreover, bioadhesive properties of polymeric ultrathin film would allow stable adhesion to the wall of an organ or of a mucosal tissue affected by cancer disease, thus hindering particle unspecific biodistribution. Nanocomposite thermonanofilms (TNFs) were fabricated as ultrathin flexible membranes using biocompatible and mucoadhesive polysaccharides (sodium alginate and chitosan) and poly(vinylpyrrolidone) encapsulating gold nanoshells.

Photothermal effect of TNFs was characterized, and their ability to destroy cancer cells by vaporization was evaluated on human neuroblastoma cell cultures.

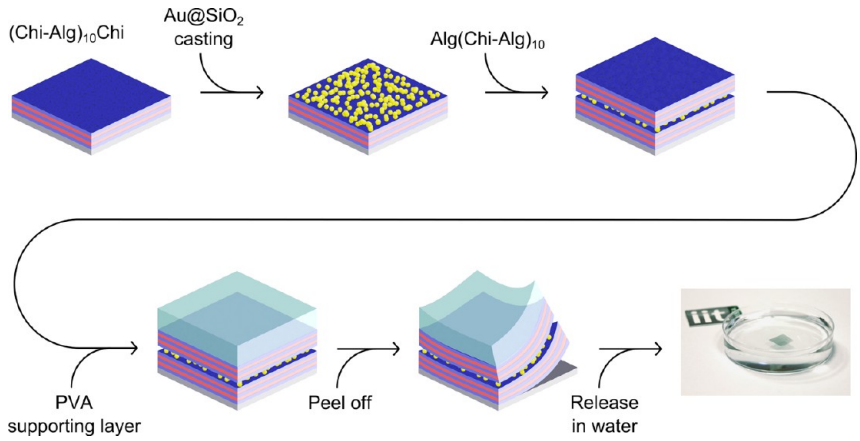

Figure 1. Preparation scheme of free-standing thermonanofilms and snapshot of nanofilm freestanding in water.

Finally, in order to predict the temperature profile, a model of particle-mediated tissue heating was introduced, which also provided a deeper insight into the obtained results.

RESULTS AND DISCUSSION

Thermonanofilm Morphology. The nanocomposite thermonanofilms have been developed by drop casting of gold core−shell nanoparticles (Au@SiO_2) on a self-assembled electrostatic layer-by-layer thin polymeric films based on alternating layers of chitosan and sodium alginate (ChiAlg-LbL) and released in liquid by using supporting layer technique (see Figure 1 and experimental section for further details). Freestanding films could be recollected on a copper grid while retaining their structural integrity (Figure S1, Supporting Information). In order to promote the adhesion of core−shell nanoparticles with layer-by-layer film, poly(vinylpyrrolidone) (PVP) is used as particle coating. Since PVP and chitosan can assemble in gels through hydrogen bonding,[57] the coated core−shell nanoparticles (Au@SiO_2−PVP) exploit this interaction showing a better adhesion to the substrate. The fabrication process, based on encapsulation of gold nanoshells *via* drop casting in a layer-by-layer assembly, has been chosen in order to better control nanoparticles concentration and distribution inside the nanofilm. Drop casting of particles onto the surface of the nanofilm ensure good control of gold nanoshells deposition at high concentration, a key point to control thermalization process. Other spin coating procedures already presented in the literature do not allow fine control of particle quantity and arrangement inside the film, especially at high nanoparticle concentration. Moreover the spin assisted layer-by-layer provide, with respect to direct spin coating deposition, a superior thickness controllability, making possible a better compromise between film thickness (adhesive properties) and film mechanical properties.

Casting deposition from 0.05 mg mL^{-1} dispersions produced stable and spatially homogeneous adhesion of Au@SiO_2−PVP on top of ChiAlg-LbL, even after two spin washing steps and further deposition of 10.5 chitosan and sodium alginate layers, with a total surface coverage of 11 ± 1% (Figure 2A). We refer to this sample as TNF1x.

Casting more concentrated dispersions (0.5 mg mL^{-1}) on ChiAlg-LbL led to substantial increase in particle surface coverage (about 29 ± 2%), but smaller than expected if we consider that the particle amount is 10 times higher than in TNF1x samples. This is probably due to edge effect of drop casting procedure that led to a greater accumulation and aggregation of particle at the border of the samples. We refer to this concentrated sample as TNF10x (Figure 2B).

It is important to report that we found that the casting procedure is quite sensitive to several parameters (substrate surface roughness, annealing processes, presence of impurity, *etc.*), and in particular to the nanoparticle aging. We have in fact experienced that the use of aged nanoparticle (*e.g.*, few weeks aged) led to the formation of very inhomogeneous particle dispersion and strong particle aggregation. In fact, casting concentrated dispersions of aged nanoparticle (0.5 mg mL^{-1}) on ChiAlg-LbL led to a drastic reduction of particle surface coverage (about 15 ± 2%), with respect to the homogeneous TNF10x sample, due to the precipitation of big nanoparticle clusters. We refer to this inhomogeneous sample as TNF10xA (Figure 2C).

Particle clustering for TNF10xA was confirmed by AFM scans (Table 1) showing the formation of particle aggregates with an average area of 1.3 μm^2. Clusters contributed to 97% of surface coverage due to nanoshells. However, maximum height of clusters was found to be lower than 500 nm, probably due to removal of larger clusters by spin washing and subsequent spin deposition of polysaccharides.

In case of aged particles the addition of poly(vinyl alcohol) (PVA) to the concentrated dispersions improved the stability of the colloids, reducing the formation of clusters and resulting again in a homogeneous particle adhesion with a surface coverage of

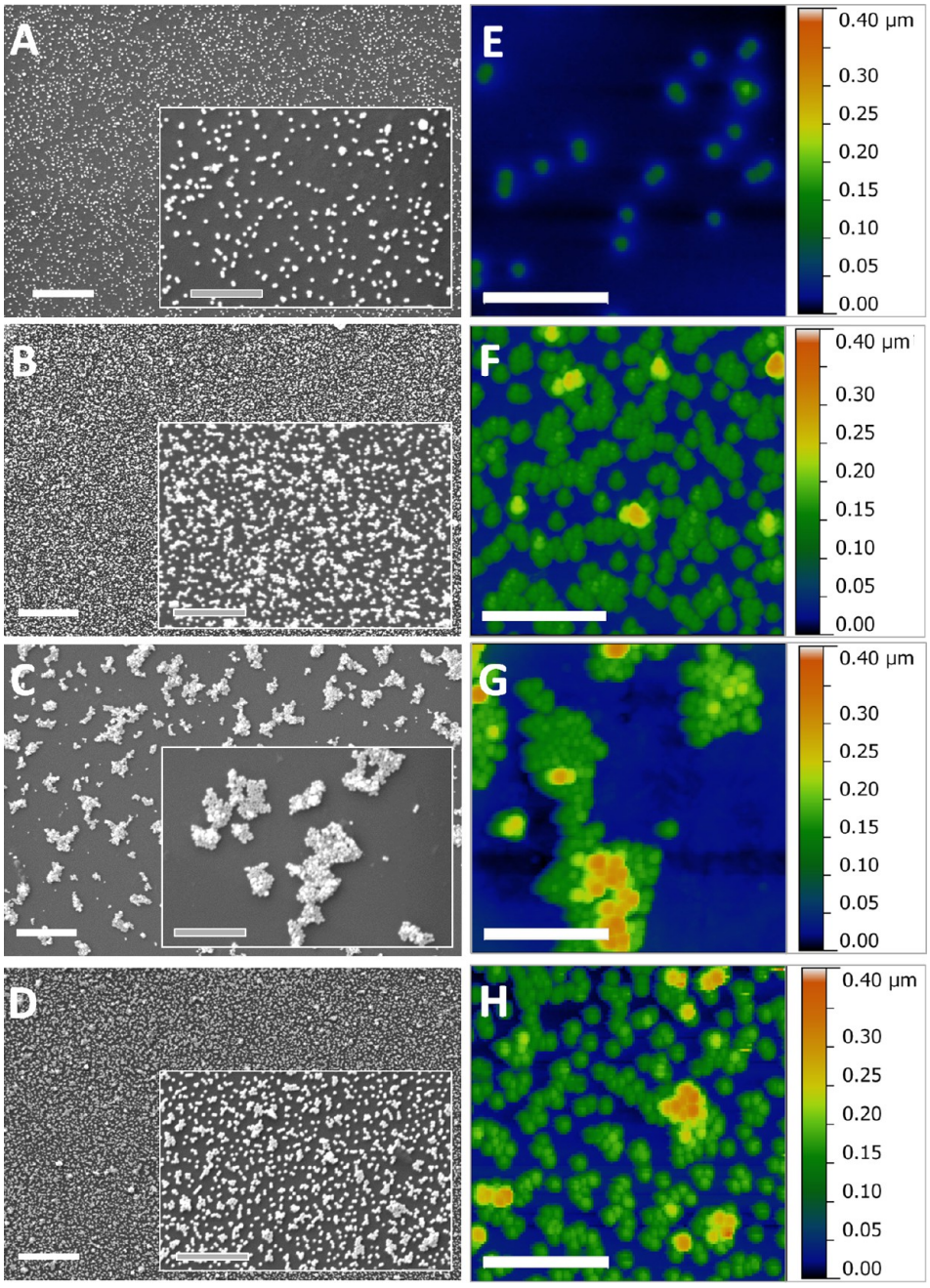

Figure 2. Morphological characterization of a TNF. SEM images of TNF1x (A), TNF10x (B), TNF10xA (C), and TNF10x with PVA (D) with a magnification of 3.9 kX (scale bars 10 μm). Inset images are referred to the same sample with a magnification of 11.3 kX (scale bars 4 μm). AFM scans of TNF1x (E), TNF10x (F), TNF10xA (G), and TNF10x with PVA (H) confirm particle arrangement and clustering inside polysaccharide matrix and enhanced homogeneity of particle disposition in the case of TNF10xA (scale bars 2 μm).

28 ± 3% (sample TNF10x with PVA, Figure 2D). Enhanced colloidal stability during casting procedure was confirmed by AFM images, which revealed a drastic decrease in cluster size, confirmed by an average cluster area of 0.36 μm^2, substantially decreased respect to TNF10xA sample, due to PVA addition to the dispersant medium. It is important to highlight that TNF10x prepared with fresh nanoparticles or with aged nanoparticles adding PVA indeed show similar properties (See Table 1 and Table S1, Supporting Information).

Since nanofilm adhesion to solid surfaces and mucosal tissues strongly depends on its thickness and surface morphology (films with an average thickness higher than 200 nm and micrometric features tend to slip and to detach from surfaces after the application),[43] all studied nanofilms have an average thickness lower than 150 nm and a nanometric average surface roughness (see Table S1, Supporting Information).

Freestanding TNFs are obtained adding, as final fabrication step, a thick PVA layer that makes possible

their peeling-off from the silicon substrate and the release in water. Once the PVA supporting layer was completely dissolved, TNFs were mechanically stable, ultraconformable, and flexible, so that they were undamaged even after aspiration and ejection with a glass pipet.

Thermonanofilm-Mediated Heating of Solid Surfaces. TNFs can be easily recollected from water on several substrates. Once dried they show strong adhesion to the substrate, even after subsequent water immersion or rinsing processes. An alternative way to apply the TNFs to different substrates is to put them (with the PVA supporting layer) in contact with the surface, and then to proceed to the dissolution of the supporting layer with water. In order to evaluate the photothermal functionality, a TNF was recollected on polystyrene (PS) substrate and then exposed to 785 nm NIR laser. Absorption spectrum of gold nanoshells indicates strong absorbance at the excitation wavelength (Figure S2, Supporting Information). Laser exposure generates deformation of the interested area (Figure 3A−D), indicating alteration of PS physical properties, already after 1 s, a shorter time than that one required to achieve quasistatic thermal conditions on the irradiated area (~10 s). An increase in laser power extended the affected area, confirming the possibility to control heating and surface morphology changes.

TABLE 1. Nanoparticle Clusters Arrangement Inside Polysaccharides Matrix

sample	Au@SiO_2−PVP surface coverage [%]	surface coverage due to clusters [%]	average cluster area [μm^2]
TNF1x	11 ± 1	65 ± 3	0.12 ± 0.02
TNF10x	29 ± 2	93 ± 2	0.38 ± 0.02
TNF10xA	15 ± 2	97 ± 3	1.3 ± 0.8
TNF10x + PVA	28 ± 3	91 ± 3	0.4 ± 0.1

AFM scans of irradiated sites confirm PS deformation, with material build-up on the sides of the exposition spot affecting the PS surface (<3 μm) due to polymer softening and subsequent cooling, and indicate a narrowly localized heating (Figure 3H). Polystyrene glass transition temperature is 100 °C;[58] however, thermal imaging underestimates photothermal effect, since the maximum temperature measured after reaching a thermal steady state was lower than 60 °C in all cases (Figure 3E). The effect is due to the limited thermal camera resolution (22.3 μm px^{-1}), to the lower irradiation angle in the case of thermal imaging, and finally to the difficulty in focusing a very thin heating layer. Nevertheless, it is worth noting that the variation in maximum temperature recorded on thermal frames linearly increases with nominal laser power (Figure 3E), indicating a very precise tuning of the photothermal effect. Temperature rise in TNFs adherent to solid surface can be as fast as 200 °C s^{-1}, so that surface deformation occurs in less than a second. This allows a controlled dynamic irradiation of TNFs on PS surfaces, performed by moving the microscope stage in predetermined paths (Figure 3F,G). The features of the thermally impressed paths depend on laser power, distribution and concentration of gold nanoshells in the TNF. Patterns impressed on TNF10xA samples are characterized by irregular width and by the presence of discontinuities, due to particle clustering and inhomogeneous particle dispersion, with cluster separation distance comparable with the laser spot size (Figure 3F). TNF10x irradiation results in regular, continuous impressions thanks to the more homogeneous arrangement of gold nanoshells within the polymer matrix during solvent evaporation. The higher particle surface density increases absorption and consequent photothermal effect, resulting in a wider melted area. Surface thermalization mediated by TNFs can be performed by finely tuning the temperature with laser

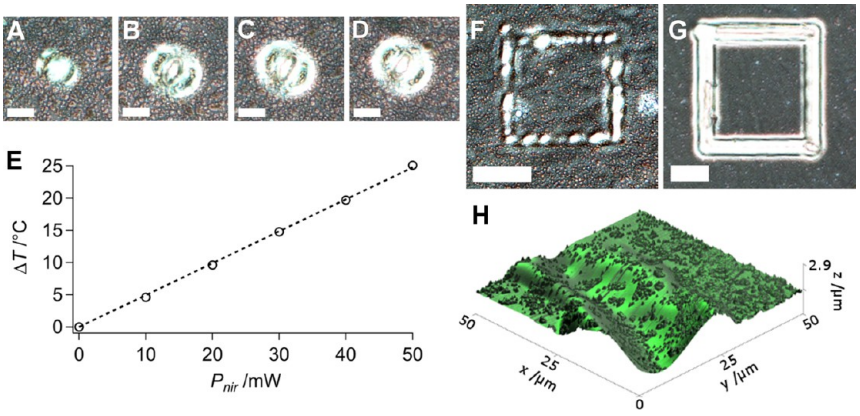

Figure 3. Effects of NIR laser exposition onto thermonanopatch. (A−D) Optical microscope images of a PS supported TNF10x exposed for 1 s to 20 (A), 30 (B), 40 (C), and 50 mW (D) NIR laser (λ = 785 nm) (scale bars 20 μm). (E) Maximum temperature increase dependence on nominal laser power for a PS supported TNF10x; dashed line is a linear fit. (F,G) Optical microscope images of a geometrical shape generated after dynamic laser exposition (25 mW) of a TNF10xA nanofilm (F) and of a TNF10x nanofilm (G) adherent onto a PS surface (scale bars 40 μm). (H) 3D rendering of an AFM scan over a PS deformation generated by laser exposure (50 mW) of a supported TNF10x.

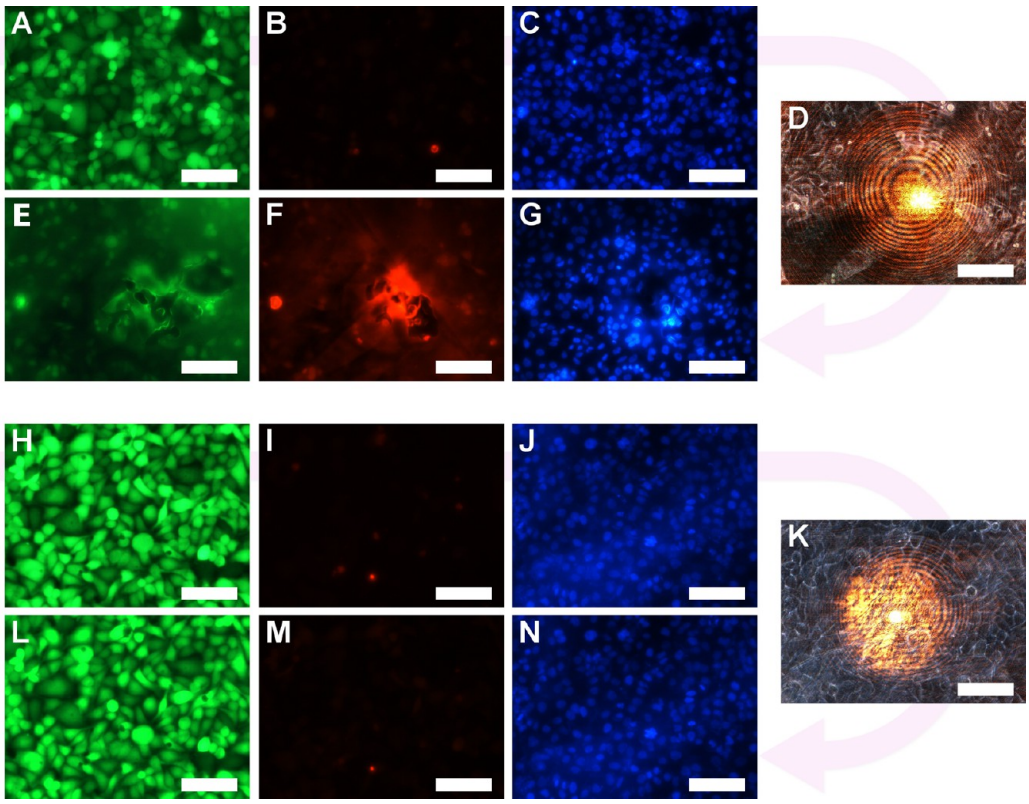

Figure 4. Cell viability assay: calcein, EthD-1, and Hoechst 33342 signal before (A,B,C) and after (E,F,G) laser exposure (λ = 785 nm, 50 mW, 150 s) of TNF10x in contact with human neuroblastoma cells. Calcein, EthD-1, and Hoechst 33342 signal before (H,I,J) and after (L,M,N) laser exposure (λ = 785 nm, 50 mW, 150 s) of a blank nanofilm as negative control sample. Bright field images of cell culture during laser exposition; the laser spot can be visualized using the CCD sensor of the inverted microscope (D,K). All scale bars = 50 μm.

output power and directing the photothermal effect in desired areas of the TNF with a micrometric resolution.

Thermonanofilm-Mediated Heating of Neuroblastoma Cancer Cells. A cell viability assay has been carried out in order to show the effect of TNF-mediated thermalization *in vitro* following NIR laser irradiation. For this test, human neuroblastoma cells have been exposed to NIR laser in the presence of gold nanoshell-loaded nanofilm; as negative control, unloaded nanofilm has been used. Figure 4A,E shows as laser effect attenuates green fluorescence intensity (due to calcein, which labels viable cells) and also causes damage to the nanofilm structure (as it is possible to notice by the swelling of the polymeric matrix distorting the green fluorescence signal). These effects demonstrate the ability of TNF to increase the temperature in the cell culture medium under NIR laser exposure. Moreover, by looking at Figure 4B,F, it is possible to notice a drastic increment of red fluorescence signal due to EthD-1 (that labels necrotic cells) in all the acquired field, but indeed especially close to the area exposed to the NIR laser. This occurrence demonstrates that TNF is able to destroy the cells following laser treatment, as demonstrated by the penetration of EthD-1 into cells with compromised membranes (EthD-1 is excluded from viable cells, since it cannot cross intact membranes).

Further information about cell viability following the treatment can be deduced by the observation of nucleus staining, which reveals an area of strongly damaged nuclei close to the laser action, surrounded by a peripheral low-intensity blue signal stemming from residual material of the destroyed nuclei (Figure 4F). These serious damages to cellular structures confirm complete cell death following thermal ablation.

Such results were obtained by TNF10x, whereas TNF1x showed no effects onto cell viability following NIR laser irradiation. This result may be attributed to low gold nanoshells amount loaded inside TNF1x polysaccharide matrix, which produces insufficient heating effects for obtaining cellular structure damages.

Moreover, negative control confirms that NIR laser is not absorbed by neither the biological tissue nor by the "blank" nanofilm. Indeed, no evidence of damage is revealed on both cell membrane and cell nuclei after laser exposure (Figure 4H–J,L–N) in the presence of an unloaded nanofilm. Calcein signal shows that cell viability is not altered by the action of the NIR laser; moreover, EthD-1 and Hoechst 33342 signals confirm intact cells after laser exposition.

Thermonanofilm-Mediated Heating of *Ex Vivo* Animal Tissue. Photothermalization of chicken breast tissue mediated

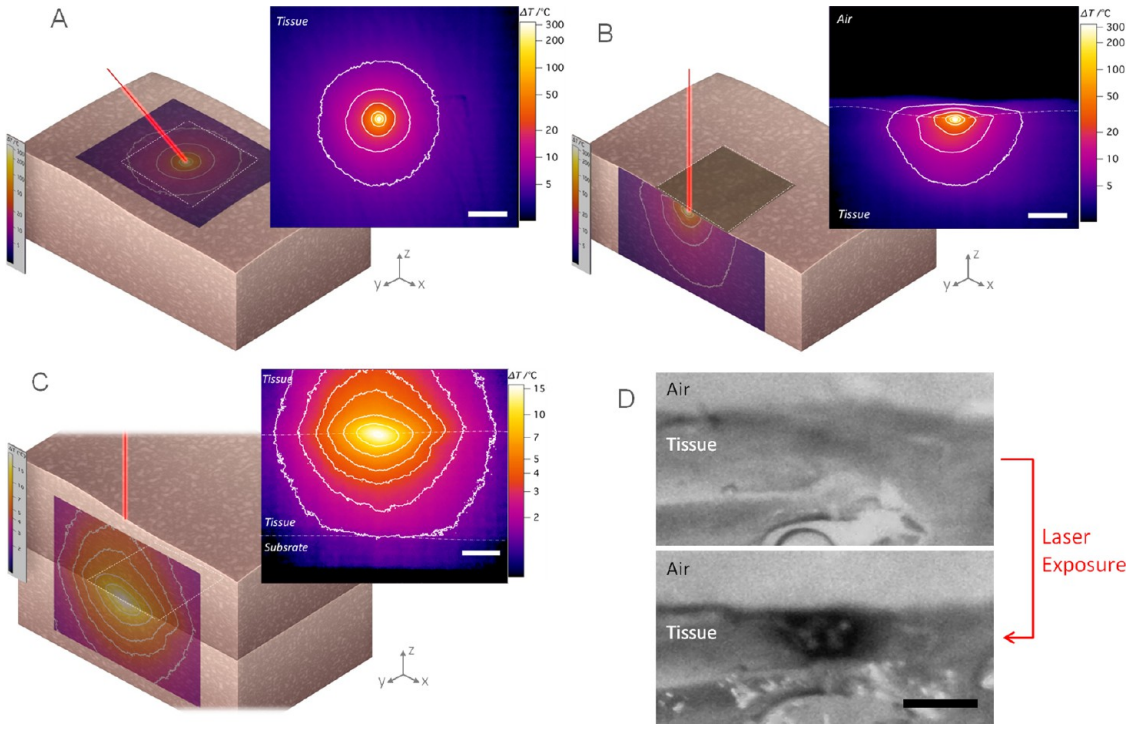

Figure 5. TNF-mediated thermalization of chicken breast tissue upon irradiation with NIR laser (808 nm) of a TNF10x adherent on the tissue surface. Temperature distribution on a plane parallel to the laser propagation direction and perpendicular to the film surface (laser power 55 mW) (A), on the tissue/TNF/air interface (laser power 55 mW) (B), and on plane perpendicular to the film surface sandwiched between two tissue slides (laser power 120 mW) (C). (D) Image of chicken breast tissue section before and after laser exposure. (All scale bars = 1 mm).

by TNF was also investigated by using a NIR laser (λ = 808 nm), for the test-cases illustrated in Figure 5, by using a power of 55 mW focused on a spot of about 100 μm of diameter. A sharp rise in temperature on the TNF/tissue interface in the configuration of Figure 5A was observed upon turning the laser on: temperature increased from room temperature T_∞ = 24.3 °C to about 360 °C with a maximum heating rate around 2000 °C s^{-1}. Temperature distribution on tissue surface reached a steady state in about 30 s, with a maximum value of 360 °C at the center of the irradiated spot. Farther from the spot center, isothermal contours were approximately circular (Figure 5A); for instance, the 100 °C contour was obtained at an average radial distance of 110 μm, while the radius of the 50 °C contour was around 200 μm. Temperatures over 300 °C cause tissue vaporization, while tissue carbonization is observed over 100 °C; both effects were indeed observed in our experiment, through the darkening of the laser spot region and the associated production of smoke during irradiation. The 50 °C contour is also representative, since above this temperature irreversible cell damage is induced, by reduction of enzyme activity, protein denaturation and increase in cell membrane stress.[59] By decreasing radiation power it is possible to achieve milder thermal effects on the exposed tissue, since temperature rise depends on NIR laser output power as shown in Figure 3E.

In addition, a simple model was introduced for describing the steady-state temperature distribution on tissue (see Section S1 of Supporting Information for all the details), with the main aim of better characterizing the considered test-case. In particular, after estimating that a significant overlap occurs among thermal boundary layers of the irradiated particles, the irradiated spot was modeled as a tiny sphere in thermal exchange (conduction) with air and tissue. A spherical approximation was nevertheless adopted, for simplicity, based on an averaged thermal conductivity coefficient $\kappa = (\kappa_t + \kappa_a)/2$, where subscripts a and t respectively denote air and chicken breast tissue. The resulting expression for the radial temperature trend reads

$$T(r) = T_\infty + \frac{\alpha P_{NIR}}{4\pi\kappa}\frac{1}{r} \quad (1)$$

where T_∞ represents tissue temperature in the far-field (unperturbed tissue at room temperature), and P_{NIR} is the nominal laser power. Moreover, α is a factor that accounts for the fraction of the nominal power that is effectively absorbed by the irradiated spot. In more detail, $\alpha = 1 - \xi_{rs} - \xi_t$, where ξ_{rs} and ξ_t denote the fractions of the nominal power that are reflected/backscattered and transmitted to tissue, respectively. The latter parameters were measured, by obtaining in particular $\alpha \cong 0.41$. Furthermore, it should be noted that eq 1 predicts a linear relation between temperature

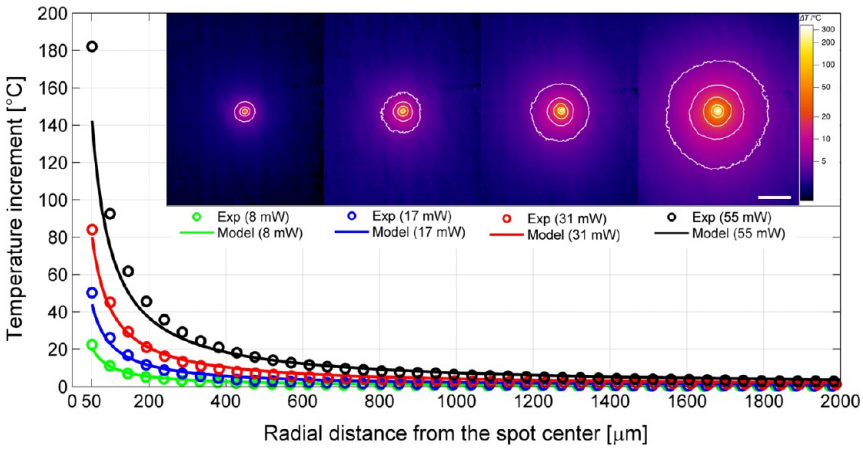

Figure 6. Radial trend of tissue temperature increment for the TNF irradiation on the *xy* plane, for selected values of the nominal power. Experimental data (circles) are compared to model predictions (solid curves).

increment $\Delta T = T - T_\infty$ and laser power P_{NIR}, as experimentally observed when assessing TNF-mediated heating of solid surfaces (Figure 3E).

Then, once adopted $\kappa_a = 0.022$ W m^{-1} K^{-1} and $\kappa_t = 0.47$ W m^{-1} K^{-1},[60] we applied eq 1 to compare model predictions with the experimental data obtained by adopting $P_{NIR} = 8$, 17, 31, and 55 mW. The considered results are shown in Figure 6. In particular, the experimental trends were obtained by processing the corresponding thermal images with Matlab (Mathworks, USA). Furthermore, the radius of the laser spot was nearly 50 μm, and the radial coordinate in Figure 6 is consistent with such a lower boundary value.

As shown in Figure 6, model predictions are in very good agreement with experimental results, minor discrepancies only arising toward the laser spot boundary, where the temperature profile is more steep (and thus hard to be accurately matched by the proposed, simple model). Indeed, the normalized error $\delta/\Delta T_{max}$ between the experimental temperature increments and the model predictions, ΔT_{max} being the maximum measured increment (occurring on the spot boundary), was equal to 0.021 $\pm$ 0.001, 0.026 $\pm$ 0.013, 0.017 $\pm$ 0.001, and 0.014 $\pm$ 0.028 (mean $\pm$ std) for the aforementioned laser powers, respectively. Moreover, the linear scaling of the temperature increment with P_{NIR} was fully confirmed. Let us then remark that, once experimentally determined α, the model at hand is fully predictive. Hence, despite the many simplifications deliberately introduced during its derivation, such a model manages to capture key effects of the involved physical parameters on tissue phototermalization, thus potentially allowing for enhanced control over the associated heating strategy.

Temperature distribution perpendicular to the TNF/tissue interface was also assessed, through the test-case illustrated in Figure 5B. The resulting temperature contours in the *zx* plane, in particular on the tissue half-plane, were approximately circular (except near the interface with air), and similar to the ones achieved in the *xy* plane. In this case, the maximum temperature was around 360 °C. Thermalization was achieved over a time interval similar to the one of the *xy* experiment.

Furthermore, tissue photothermalization was also investigated for a TNF sandwiched between two tissue slices having 3 mm thickness, as depicted in Figure 5C (in this case a laser power of 120 mW was used). As expected, the obtained temperature distribution was approximately symmetrical with respect to the TNF plane. This is in agreement with the fact that heating is only produced by TNF NIR absorption. In this case, temperature contours were less trivial: their pseudo-elliptical shape was associated with a less focused NIR absorption region, the ellipticity of which was likely determined by photons scattering within tissue, prior to reaching the TNF. The maximum temperature reached for this test case was around 40 °C, and thermalization was observed after nearly 45 s. Both these figures confirm that scattering of NIR photons by overlying tissue played a major role in this experiment, in particular by causing a decay in the intensity of the incident laser beam. Nonetheless, the resulting temperature field demonstrated the possibility to localize moderate thermal effects in some depth within tissue, specifically around the TNF, *e.g.*, to achieve cell death or to facilitate other cancer therapies, without adverse thermal effects on surrounding healthy tissue. Indeed, by controlling TNF depth within a given tissue, as well as by adjusting laser output power, it is possible to modulate the obtained thermalization region around TNF, in order to accurately tune the considered photothermal treatment. Further control over the considered strategy could be provided by also considering time-dependent irradiation strategies, which however are beyond the present investigation.

To conclude, it is worth remarking that comparison with irradiation of blank NFs and bare tissue confirmed that Au@SiO_2—PVP nanoshells were fully responsible of the tissue thermalization, since no appreciable

temperature rise was recorded in the corresponding control experiments (Figure S4, Supporting Information).

CONCLUSION

Herein a new thermonanofilm for localized hyperthermia and photothermal ablative applications is presented, composed by Au@SiO_2−PVP nanoshells encapsulated inside an ultrathin polysaccharide matrix. Thermonanofilms, fabricated with mucoadhesive materials, possess unique properties of flexibility, low surface roughness, and submicrometric thickness, allowing adhesion to tissue surfaces. The nanoshell density and arrangement inside the film can be controlled by changing dispersion concentration and, in the case of aged nanoparticles, adding surfactants such as PVA, thus allowing the precise tuning of NIR/thermal conversion properties of the TNF. Temperature achievable during TNF-mediated surface photothermalization induced by NIR laser can be controlled by tuning laser power. Moreover, precisely directed heating in any part of the polymer composite is also possible by focusing and moving NIR laser onto the surface of TNF.

In vitro experiments carried out on cancer cells demonstrated the efficacy of TNF approach. In particular, cell viability experiments carried out on TNFs treated with NIR laser showed a complete thermal ablation of cancer cells, demonstrated by irreversible cell membrane damage and nuclei destruction. Moreover, negative control performed with NIR laser on unloaded nanofilms revealed absence of cell structure damage, thus demonstrating the noninvasiveness of the approach.

Further experiments carried out on *ex vivo* tissues demonstrated also the applicability of the system in a realistic scenario. In this case, thermal profile characterization showed that surface heating and cooling occur almost instantaneously and that, with a 55 mW power NIR laser in the presence of TNF temperature can reach a maximum value above 300 °C inducing surface tissue vaporization, while in the presence of control unloaded nanofilms the temperature has negligible increase, because of the low absorption of NIR photons by the tissues. Moreover, thermal profiles demonstrate that the temperature increase is localized on the tissue surface, being the Au nanoshells the only components that absorb NIR photons.

Finally, a steady-state model was proposed in order to understand the key aspect of tissue thermalization upon NIR irradiation of TNF. The model predictions are in good agreement with experimental results, and the root-mean-square error δ between model and experimental points was such that $\delta/\Delta T_{max} \cong 0.1$. These results provide useful guidelines for the development of TNFs and for the comprehension of the main factors that cause tissue thermalization. In particular, the model highlights the importance of achieving a high particle surface coverage in order to generate temperature buildup on the irradiation spot.

Thermal profile analysis of TNF sandwiched inside two tissue slides shows the possibility to localize heating nearby the area of application of the nanofilm, with a lower temperature rise compared to previous experiments, due to photon scattering. However, by increasing laser output power and exposition time, it is theoretically possible to reach the desired temperature values at a certain depth, given the thickness and composition of biological tissue overlying TNF.

All these results underline the advantage of the proposed approach with respect to traditional laser ablation, in which difficult heating effect (especially in deep application) may cause problems such as organ perforation and lesion of the underlying healthy tissues and nerves.[61,62] On the other hand, TNF-mediated thermalization of cancer tissue could be proposed as an additional strategy to chemotherapy and radiotherapy, not only for superficial lesions, but also located more deeply inside an organ. Feasible clinical scenarios could involve the application of TNF onto the oral, intestinal, gastric, vaginal, or esophageal mucosa, in order to treat tumor masses located at these sites, or for the treatment of "head and neck" cancer.[63]

METHODS

Au@SiO_2−PVP nanoshell suspension in deionized water (50 μg mL^{-1}, $2.9 \cdot 10^9$ particles/mL) was purchased from Nanocomposix, San Diego, CA. These particles have a core diameter of 120 nm and a shell thickness of 15 nm, showing a strong NIR light absorption, with a maximum absorbance peak at about 800 nm.

For *in vitro* experiments cell culture reagents were purchased from Euroclone and the LIVE/DEAD viability/cytotoxicity kit was purchased from Molecular Probes.

Fabrication of Polysaccharide/Gold Nanoshell Nanofilm. Polysaccharide/gold nanoshell nanofilms (thermonanofilms, TNFs) were fabricated by spin-assisted layer-by-layer assembly (SA-LbL) of polysaccharides and casting deposition of gold nanoshells. A schematization of the fabrication is given in Figure 1. Silicon wafers (400 μm thick, *p* type, boron doped, ⟨100⟩ Si-Mat Silicon Materials, Kaufering, Germany), used as substrates for film deposition, were cut (2 cm × 2 cm) and cleaned using Nanostrip (Cyantek, Fremont, CA) at 120 °C for 10 min and then washed with deionized (DI) water (18 MΩ cm) in order to remove dust and impurities. A sodium alginate solution in DI water (1 mg mL^{-1}, 106 kDa, Nacalai Tesque, Kyoto, Japan) and a chitosan solution in 1% acetic acid (1 mg mL^{-1}, 88 kDa, Nacalai Tesque) were filtered with 0.45 μm pores membrane filters and used for the SA-LbL film fabrication. A drop of chitosan solution (200 μL) was placed onto the Si wafer and spin coated at 4500 rpm for 20 s and then washed twice with a drop of DI water (300 μL) spin coated at 4500 rpm for 20 s. Then, a drop of sodium alginate (200 μL) was placed onto the chitosan layer, spin-coated at 4500 rpm for 20 s, and washed twice with a drop of deionized water spin coated at 4500 rpm for 20 s. This procedure was repeated 10 times, and after this another

chitosan layer was deposited following the same procedure. Casting deposition of gold nanoshells on top of the LbL polysaccharide film was performed using a drop of Au@SiO_2-PVP suspension (300 μL, 0.05 mg mL^{-1}). In order to increase particle loading, concentrated dispersions were also prepared and casted on LbL films. The original dispersion was concentrated by centrifugation at 2500 rpm for 10 min. After removal of excess water, precipitated nanoshells were resuspended with deionized water or with a 60 μg mL^{-1} water solution of poly(vinyl alcohol) (PVA, Kanto Chemicals, Tokyo, Japan), to obtain 0.5 mg mL^{-1} nanoshell dispersions. After evaporation of gold nanoshell dispersant, the surface of the nanofilms was rinsed five times with 1 mL of DI water in order to remove unbound nanoshells and dissolve PVA. Sample surface was spin cleaned two times with water and then covered with a sodium alginate layer and other 10 polysaccharide bilayers. Sample obtained by casting the original dispersion, the concentrated dispersion, and the PVA concentrated dispersion are designated as TNF1x, TNF10x, and TNF10x with PVA, respectively. Blank samples, *i.e.*, 21-pairs unloaded polysaccharide films, were prepared as negative controls for irradiation experiments. Finally, a drop of PVA aqueous solution (500 μL, 100 mg mL^{-1}) was placed onto each nanofilm and spin coated at 3000 rpm for 60 s in order to create a water-soluble supporting layer used to remove the polymer nanofilm from silicon substrate by peeling it off with tweezers after cutting its borders. Nanofilms were then ready to be transferred and manipulated.

Morphological Characterization of TNFs. Surface characterization of wafer supported TNFs and TNFs adhered on poly(styrene) (PS) was performed by atomic force microscopy with an Innova SPM (Bruker, Billerica, MA). 50 × 50, 20 × 20, and 5 × 5 μm^2 AFM scans were performed in tapping mode, using MikroMasch NSC35/AlBS aluminum-coated *n* type silicon probes (Innovative Solutions Bulgaria, Sofia, Bulgaria) with a resonance frequency of 150−200 kHz and a force constant of 5−16 N m^{-1}. Grain analysis was performed on 20 × 20 μm^2 scans of TNFs. Nanoshells were marked on the resulting images by height thresholding. Grains with a projected area lower than 0.08 μm^2 were not considered in cluster statistics, since they corresponded to single particles. This value is larger than the theoretical projected area of adhered nanoshells (0.015 μm^2), due to scanning probe convolution, presence of the PVP coating, and coverage with LbL bilayers.

TNF thickness was evaluated on wafer supported films scratched with metal tweezers. Height profiles spanning the scratch were recorded using a P6 stylus profilometer (KLA-Tencor, Milpitas, CA). Scanning electron microscopy (SEM) images were acquired with an EVO MA 10 (Carl Zeiss, Oberkochen, Germany) at 3.9k× and 11.3k× magnification using an acceleration voltage of 10 kV. Before SEM, samples were coated with a Au layer (8 nm) using a Q150R BS sputter coater (40 mA, 10 Pa, 60 s, Quorum Technologies, West Sussex, UK). Particles surface coverage has been calculated using an imaging software (ImageJ) based on 5 different SEM images for each sample.

Photothermalization of TNFs. For preliminary evaluation of TNF-mediated photothermalization, PVA supported TNFs (TNF10x and TNF10xA) were placed on the bottom of a (PS) Petri dish. After dissolution of the supporting layer by rinsing the sample with DI water, TNFs were dried and then exposed to NIR radiation by means of a OBIS 785 LX laser source (λ = 785 nm, Coherent, Santa Clara, CA) connected to an *Ti*-E inverted fluorescence microscope (Nikon, Tokio, Japan) through the photoactivation laser port. Irradiation was carried out for 1 s with nominal laser power varied between 10 and 50 mW through OBIS Remote controller and OBIS Connection control software (Coherent). Temperature variation with laser power was measured with an A325sc thermal camera (FLIR Systems, Wilsonville, OR) with a close-up lens (T197415, FLIR Systems) featuring an 8 × 6 mm^2 field of view and a spatial resolution of 25 μm. For these measurements, samples were tilted by 45° respect to the microscope stage plane, in order to accommodate for both the thermal camera optics and for the microscope light source. In controlled dynamic exposure experiments, samples were moved relatively to the laser spot using the motorized microscope stage. Images of the sample were acquired with NIS Elements imaging software (Nikon), before and after exposure. *In vitro* cell photothermalization was carried out using freestanding TNFs (TNF1x, TNF10x and unloaded nanofilms). Each TNF was detached from silicon substrates, dipped into PBS in order to dissolve the PVA supporting layer and transferred from the buffer solution to the well containing the cells using a Pasteur pipet. Buffer was removed until 200 μL of liquid remained in each well, so that TNF was in contact with the neuroblastoma cell culture. Each sample was irradiated with the OBIS 785 LX laser source (50 mW, 150 s).

Cell Culture, Viability Assay, and *In Vitro* Ablation Experiment. Human neuroblastoma SH-SY5Y cells (ATCC CRL-2266) were cultured in Dulbecco's modified Eagle's medium and Ham's F12 (1:1) with 10% fetal bovine serum, 100 IU mL^{-1} of penicillin, 100 μg mL^{-1} of streptomycin and 2 mM of L-glutamine. Cells were maintained at 37 °C in a saturated humidity atmosphere containing 95% air/5% CO_2.

Viability of cells before and after laser stimulation was investigated with the LIVE/DEAD viability/cytotoxicity kit (Molecular Probes, Life Technologies, Carlsbad, CA). The kit contains calcein AM (4 mM in anhydrous DMSO) and ethidium homodimer-1 (EthD-1, 2 mM in DMSO/H_2O 1:4 (v/v)), which allow live cell in green and dead cells in red to be stained, respectively. Moreover, the addiction of Hoechst 33342 (5 μg mL^{-1}) to cells culture medium allows nucleus staining (in blue). Cells were pretreated for 5 min at 37 °C with 2 mM of calcein AM and 4 mM of EthD-1 in PBS.

Ex vivo experiments were carried out on TNFs attached to the surface of a sample tissue (chicken breast, *Gallus gallus domesticus*). A rectangular tissue section (2 × 3 cm) with a thickness of about 3 mm was cut and placed on a glass slide. TNF10x and a blank NF were peeled from their silicon substrate and placed on top of the tissue, and then the PVA supporting layer was washed away with DI water. The tissue was placed on an XYZ adjustable sample holder to be irradiated with an RLTMDL-808−500 NIR laser source (λ = 808 nm, maximum output power 500 mW, Roithner Lasertechink, Vienna, Austria) in the configuration shown in Figure S3 (Supporting Information). Absorption by Au@SiO_2−PVP nanoshells is not sensitive to the change in stimulation wavelength with respect to the microscope laser, due to their very broad NIR absorption peak (Figure S1, Supporting Information). Laser radiation was coupled to a multimode optical fiber with a 600-μm-diameter core. A three lens system (lenses from Thorlabs, Inc.) composed of an ACN254−050-B and an AC254−075-B (separated by a 28 mm air gap) forming a collimating system with an effective focal length of approximately 300 mm, and an AC254−050-B as a focusing element, was designed to focus the radiation output by the fiber into a 100-μm-diameter spot on the sample. Laser power measurement and scattered/reflected power estimation were performed by means of a calibrated S121C Photodiode coupled to a PM100D power meter (Thorlabs Inc.).

Temperature profiles were acquired with the A325sc thermal camera on the TNF plane and perpendicularly to the TNF. Irradiation of a tissue−TNF−tissue sandwich was performed, in order to evaluate the effects of NIR laser tissue scattering and absorption on TNF-mediated thermalization. Thermal profiles were analyzed using FLIR ResearchIR MAX software (FLIR Systems) and Igor Pro 6 (Wavemetrics, Lake Oswego, OR).

Conflict of Interest: The authors declare no competing financial interest.

Supporting Information Available: Thickness and roughness of the different TNFs, SEM scan of a freestanding TNF10x collected on a TEM copper grid, absorbance spectra of Au@SiO_2−PVP nanoshells and of the TNF composites, illustration of experimental setups for laser irradiation experiments, thermal images of irradiated *ex vivo* control samples, model of TNF-mediated heating of animal tissue description. This material is available free of charge *via* the Internet at http://pubs.acs.org.

REFERENCES AND NOTES

1. Cherukuri, P.; Glazer, E.; Curley, S. Targeted Hyperthermia Using Metal Nanoparticles. *Adv. Drug Delivery Rev.* **2010**, *62*, 339–345.

2. Brannon-Peppas, L.; Blanchette, J. O. Nanoparticle and Targeted Systems for Cancer Therapy. *Adv. Drug Delivery Rev.* **2012**, *64*, 206–212.
3. Storm, F. K.; Harrison, W. H.; Elliott, R. S.; Morton, D. L. Normal Tissue and Solid Tumor Effects of Hyperthermia in Animal Models and Clinical Trials. *Cancer Res.* **1979**, *39*, 2245–2251.
4. Wust, P.; Hildebrandt, B.; Sreenivasa, G.; Rau, B.; Gellermann, J.; Riess, H.; Felix, R.; Schlag, P. M. Hyperthermia in Combined Treatment of Cancer. *Lancet Oncol.* **2002**, *3*, 487–497.
5. Vora, N.; Forell, B.; Joseph, C.; Lipsett, J.; Archambeau, J. O. Interstitial Implant with Interstitial Hyperthermia. *Cancer* **1982**, *50*, 2518–2523.
6. Turner, P. F. Regional Hyperthermia with an Annular Phased Array. *IEEE Trans. Biomed. Eng.* **1984**, *BME-31*, 106–114.
7. Philipp, C. M.; Rohde, E.; Berlien, H. Nd: YAG Laser Procedures in Tumor Treatment. *Seminars in Surgical Oncology.* **1995**, *11*, 290–298.
8. Cakir, B.; Ugras, N. S.; Gul, K.; Ersoy, R.; Korukluoglu, B. Initial Report of the Results of Percutaneous Laser Ablation of Benign Cold Thyroid Nodules: Evaluation of Histopathological Changes after 2 Years. *Endocr. Pathol.* **2009**, *20*, 170–176.
9. Tateishi, R.; Shiina, S.; Teratani, T.; Obi, S.; Sato, S.; Koike, Y.; Fujishima, T.; Yoshida, H.; Kawabe, T.; Omata, M. Percutaneous Radiofrequency Ablation for Hepatocellular Carcinoma. An Analysis of 1000 Cases. *Cancer* **2005**, *103*, 1201–1209.
10. Zhang, L.; Zhu, H.; Jin, C.; Zhou, K.; Li, K.; Su, H.; Chen, W.; Bai, J.; Wang, Z. High-Intensity Focused Ultrasound (HIFU): Effective and Safe Therapy for Hepatocellular Carcinoma Adjacent to Major Hepatic Veins. *Eur. Radiol.* **2009**, *19*, 437–445.
11. Brigger, I.; Dubernet, C.; Couvreur, P. Nanoparticles in Cancer Therapy and Diagnosis. *Adv. Drug Delivery Rev.* **2012**, *64*, 24–36.
12. Maeda, H.; Wu, J.; Sawa, T.; Matsumura, Y.; Hori, K. Tumor Vascular Permeability and the EPR Effect in Macromolecular Therapeutics: A Review. *J. Controlled Release* **2000**, *65*, 271–284.
13. Gordon, R. T.; Hines, J. R.; Gordon, D. Intracellular Hyperthermia a Biophysical Approach to Cancer Treatment *via* Intracellular Temperature and Biophysical Alterations. *Med. Hypotheses* **1979**, *5*, 83–102.
14. Maier-Hauff, K.; Rothe, R.; Scholz, R.; Gneveckow, U.; Wust, P.; Thiesen, B.; Feussner, A.; Deimling, A.; von Waldoefner, N.; Felix, R.; *et al.* Intracranial Thermotherapy Using Magnetic Nanoparticles Combined with External Beam Radiotherapy: Results of a Feasibility Study on Patients with Glioblastoma Multiforme. *J. Neurooncol.* **2007**, *81*, 53–60.
15. Bertotti, G.; Basso, V.; Beatrice, C.; Lobue, M.; Magni, A.; Tiberto, P. Hysteresis in Magnetic Materials: The Role of Structural Disorder, Thermal Relaxation, and Dynamic Effects. *J. Magn. Magn. Mater.* **2001**, *226−230*, 1206–1212.
16. Lv, Y.-G.; Deng, Z.-S.; Liu, J. 3-D Numerical Study on the Induced Heating Effects of Embedded Micro/nanoparticles on Human Body Subject to External Medical Electromagnetic Field. *IEEE Trans. Nanobiosci.* **2005**, *4*, 284–294.
17. Jordan, A.; Scholz, R.; Wust, P.; Fähling, H.; Felix, R. Magnetic Fuid Hyperthermia (MFH): Cancer Treatment with AC Magnetic Field Induced Excitation of Biocompatible Superparamagnetic Nanoparticles. *J. Magn. Magn. Mater.* **1999**, *201*, 413–419.
18. Johannsen, M.; Gneveckow, U.; Eckelt, L.; Feussner, A.; Waldöfner, N.; Scholz, R.; Deger, S.; Wust, P.; Loening, S. A.; Jordan, A. Clinical Hyperthermia of Prostate Cancer Using Magnetic Nanoparticles: Presentation of a New Interstitial Technique. *Int. J. Hyperthermia* **2005**, *21*, 637–647.
19. Hutter, E.; Fendler, J. H. Exploitation of Localized Surface Plasmon Resonance. *Adv. Mater.* **2004**, *16*, 1685–1706.
20. Link, S.; El-Sayed, M. A. Shape and Size Dependence of Radiative, Non-Radiative and Photothermal Properties of Gold Nanocrystals. *Int. Rev. Phys. Chem.* **2000**, *19*, 409–453.
21. Schwartzberg, A. M.; Zhang, J. Z. Novel Optical Properties and Emerging Applications of Metal Nanostructures. *J. Phys. Chem. C* **2008**, *112*, 10323–10337.
22. Perez-Juste, J.; Pastoriza-Santos, I.; Liz-Marzán, L. M.; Mulvaney, P. Gold Nanorods: Synthesis, Characterization and Applications. *Coord. Chem. Rev.* **2005**, *249*, 1870–1901.
23. Averitt, R. D.; Westcott, S. L.; Halas, N. J. Linear Optical Properties of Gold Nanoshells. *J. Opt. Soc. Am. B* **1999**, *16*, 1824–1832.
24. Weissleder, R.; Ntziachristos, V. Shedding Light onto Live Molecular Targets. *Nat. Med.* **2003**, *9*, 123–128.
25. Hirsch, L. R.; Stafford, R. J.; Bankson, J. A.; Sershen, S. R.; Rivera, B.; Price, R. E.; Hazle, J. D.; Halas, N. J.; West, J. L. Nanoshell-Mediated near-Infrared Thermal Therapy of Tumors under Magnetic Resonance Guidance. *Proc. Natl. Acad. Sci. U. S. A.* **2003**, *100*, 13549–13554.
26. O'Neal, D. P. P.; Hirsch, L. R.; Halas, N. J.; Payne, J. D. D.; West, J. L. Photo-Thermal Tumor Ablation in Mice Using near Infrared-Absorbing Nanoparticles. *Cancer Lett.* **2004**, *209*, 171–176.
27. Day, E. S.; Thompson, P. A.; Zhang, L.; Lewinski, N. A.; Ahmed, N.; Drezek, R. A.; Blaney, S. M.; West, J. L. Nanoshell-Mediated Photothermal Therapy Improves Survival in a Murine Glioma Model. *J. Neurooncol.* **2011**, *104*, 55–63.
28. Huang, X.; Jain, P. K.; El-Sayed, I. H.; El-Sayed, M. A. Plasmonic Photothermal Therapy (PPTT) Using Gold Nanoparticles. *Lasers Med. Sci.* **2008**, *23*, 217–228.
29. Eck, W.; Craig, G.; Sigdel, A.; Ritter, G.; Old, L. J.; Tang, L.; Brennan, M. F.; Allen, P. J.; Mason, M. D. PEGylated Gold Nanoparticles Conjugated to Monoclonal F19 Antibodies as Targeted Labeling Agents for Human Pancreatic Carcinoma Tissue. *ACS Nano* **2008**, *2*, 2263–2272.
30. Ferrari, M. Cancer Nanotechnology: Opportunities and Challenges. *Nat. Rev. Cancer* **2005**, *5*, 161–171.
31. Peer, D.; Karp, J. M.; Hong, S.; Farokhzad, O. C.; Margalit, R.; Langer, R. Nanocarriers as an Emerging Platform for Cancer Therapy. *Nat. Nanotechnol.* **2007**, *2*, 751–760.
32. Khlebtsov, N.; Dykman, L. Biodistribution and Toxicity of Engineered Gold Nanoparticles: A Review of *In Vitro* and *In Vivo* Studies. *Chem. Soc. Rev.* **2011**, *40*, 1647–1671.
33. Jain, R. K. Transport of Molecules, Particles, and Cells in Solid Tumors. *Annu. Rev. Biomed. Eng.* **1999**, *1*, 241–263.
34. Cole, A. J.; Yang, V. C.; David, A. E. Cancer Theranostics: The Rise of Targeted Magnetic Nanoparticles. *Trends Biotechnol.* **2011**, *29*, 323–332.
35. Jong, W. H. De; Hagens, W. I.; Krystek, P.; Burger, M. C.; Sips, A. J. A. M.; Geertsma, R. E. Particle Size-Dependent Organ Distribution of Gold Nanoparticles after Intravenous Administration. *Biomaterials* **2008**, *29*, 1912–1919.
36. Xie, G.; Sun, J.; Zhong, G.; Shi, L.; Zhang, D. Biodistribution and Toxicity of Intravenously Administered Silica Nanoparticles in Mice. *Arch. Toxicol.* **2010**, *84*, 183–190.
37. Kunzmann, A.; Andersson, B.; Thurnherr, T.; Krug, H.; Scheynius, A.; Fadeel, B. Toxicology of Engineered Nanomaterials: Focus on Biocompatibility, Biodistribution and Biodegradation. *Biochim. Biophys. Acta* **2011**, *1810*, 361–373.
38. Choi, H.; Frangioni, J. Nanoparticles for Biomedical Imaging: Fundamentals of Clinical Translation. *Mol. Imaging* **2010**, *9*, 291–310.
39. Yu, T.; Hubbard, D.; Ray, A.; Ghandehari, H. *In Vivo* Biodistribution and Pharmacokinetics of Silica Nanoparticles as a Function of Geometry, Porosity and Surface Characteristics. *J. Controlled Release* **2012**, *163*, 46–54.
40. Krishnan, S.; Diagaradjane, P.; Sang, C. Nanoparticle-Mediated Thermal Therapy: Evolving Strategies for Prostate Cancer Therapy. *Int. J. Hyperthermia* **2010**, *26*, 775–789.
41. Matteini, P.; Ratto, F.; Rossi, F.; Centi, S. Chitosan Films Doped with Gold Nanorods as Laser Activatable Hybrid Bioadhesives. *Adv. Mater.* **2010**, *22*, 4313–4316.
42. Fujie, T.; Okamura, Y.; Takeoka, S. Ubiquitous Transference of a Free-Standing Polysaccharide Nanosheet with the Development of a Nano-Adhesive Plaster. *Adv. Mater.* **2007**, *19*, 3549–3553.

43. Fujie, T.; Furutate, S.; Niwa, D.; Takeoka, S. A Nano-Fibrous Assembly of Collagen-Hyaluronic Acid for Controlling Cell-Adhesive Properties. *Soft Matter* **2010**, *6*, 4672–4676.
44. Fujie, T.; Saito, A.; Kinoshita, M.; Miyazaki, H.; Ohtsubo, S.; Saitoh, D.; Takeoka, S. Dual Therapeutic Action of Antibiotic-Loaded Nanosheets for the Treatment of Gastrointestinal Tissue Defects. *Biomaterials* **2010**, *31*, 6269–6278.
45. Fujie, T.; Matsutani, N.; Kinoshita, M.; Okamura, Y.; Saito, A.; Takeoka, S. Adhesive, Flexible, and Robust Polysaccharide Nanosheets Integrated for Tissue-Defect Repair. *Adv. Funct. Mater.* **2009**, *19*, 2560–2568.
46. Fujie, T.; Desii, A.; Ventrelli, L.; Mazzolai, B.; Mattoli, V. Inkjet Printing of Protein Microarrays on Freestanding Polymeric Nanofilms for Spatio-Selective Cell Culture Environment. *Biomed. Microdevices* **2012**, *14*, 1069–1076.
47. Redolfi Riva, E.; Desii, A.; Sartini, S.; Motta, C.; La Mazzolai, B.; Mattoli, V. PMMA/Polysaccharides Nanofilm Loaded with Adenosine Deaminase Inhibitor for Targeted Anti-Inflammatory Drug Delivery. *Langmuir* **2013**, *29*, 13190–13197.
48. Greco, F.; Zucca, A.; Taccola, S.; Menciassi, A.; Fujie, T.; Haniuda, H.; Takeoka, S.; Dario, P.; Mattoli, V. Ultra-Thin Conductive Free-Standing PEDOT/PSS Nanofilms. *Soft Matter* **2011**, *7*, 10642–10650.
49. Greco, F.; Zucca, A.; Taccola, S.; Mazzolai, B.; Mattoli, V. Patterned Free-Standing Conductive Nanofilms for Ultra-conformable Circuits and Smart Interfaces. *ACS Appl. Mater. Interfaces* **2013**, *5*, 9461–9469.
50. Aliev, F.; Correa-Duarte, M.; Mamedov, A. A.; Ostrander, J. W.; Giersig, M.; Liz-Marzán, L. M.; Kotov, N. A. Layer By Layer Assembly of Core Shell Magnetite Nanoparticles: Effect of Silica Coating on Interparticle Interactions and Magnetic Properties. *Adv. Mater.* **1999**, *11*, 1006–1010.
51. Malikova, N.; Pastoriza-Santos, I.; Schierhorn, M.; Kotov, N. A.; Liz-Marzán, L. M. Layer-by-Layer Assembled Mixed Spherical and Planar Gold Nanoparticles: Control of Interparticle Interactions. *Langmuir* **2002**, *18*, 3694–3697.
52. Xu, T.; Jin, J.; Gregory, C.; Hickman, J. J.; Boland, T. Inkjet Printing of Viable Mammalian Cells. *Biomaterials* **2005**, *26*, 93–99.
53. Jiang, C. Y.; Tsukruk, V. V. Freestanding Nanostructures *via* Layer-by-Layer Assembly. *Adv. Mater.* **2006**, *18*, 829–840.
54. Markutsya, S.; Jiang, C.; Pikus, Y.; Tsukruk, V. V. Freely Suspended Layer-by-Layer Nanomembranes: Testing Micromechanical Properties. *Adv. Funct. Mater.* **2005**, *15*, 771–780.
55. Vial, S.; Pastoriza-Santos, I.; Pérez-Juste, J.; Liz-Marzán, L. M. Plasmon Coupling in Layer-by-Layer Assembled Gold Nanorod Films. *Langmuir* **2007**, *23*, 4606–4611.
56. Taccola, S.; Desii, A.; Pensabene, V.; Fujie, T.; Saito, A.; Takeoka, S.; Dario, P.; Menciassi, A.; Mattoli, V. Free-Standing Poly(l-Lactic Acid) Nanofilms Loaded with Superparamagnetic Nanoparticles. *Langmuir* **2011**, *27*, 5589–5595.
57. Marsano, E.; Bianchi, E.; Vicini, S.; Compagnino, L.; Sionkowska, A.; Skopińska, J.; Wiśniewski, M. Stimuli Responsive Gels Based on Interpenetrating Network of Chitosan and Poly-(vinylpyrrolidone). *Polymer* **2005**, *46*, 1595–1600.
58. Brandrup, J.; Immergut, E. H.; Grulke, E. A. *Polymer Handbook*; John Wiley & Sons: New York, 2003.
59. Boulnois, J. Photophysical Processes in Recent Medical Laser Developments: A Review. *Lasers Med. Sci.* **1986**, *1*, 47–66.
60. Huang, L.; Liu, L.-S. Simultaneous Determination of Thermal Conductivity and Thermal Diffusivity of Food and Agricultural Materials Using a Transient Plane-Source Method. *J. Food Eng.* **2009**, *95*, 179–185.
61. Law, P.; Gedroyc, W. M.; Regan, L. Magnetic Resonance-Guided Percutaneous Laser Ablation of Uterine Fibroids. *J. Magn. Reson. Imaging* **2000**, *12*, 565–570.
62. Neukam, F. W.; Stelzle, F. Laser Tumor Treatment in Oral and Maxillofacial Surgery. *Phys. Procedia* **2010**, *5*, 91–100.
63. Upile, T.; Fisher, C.; Jerjes, W.; Maaytah, M.; El Searle, A.; Archer, D.; Michaels, L.; Rhys-Evans, P.; Hopper, C.; Howard, D. The Uncertainty of the Surgical Margin in the Treatment of Head and Neck Cancer. *Oral Oncol.* **2007**, *43*, 321–326.